Deblurring of breathing motion artifacts in thoracic PET images by deconvolution methods

Issam El Naqa,[a] Daniel A. Low, Jeffrey D. Bradley, Milos Vicic, and Joseph O. Deasy
Department of Radiation Oncology, Washington University, School of Medicine, St. Louis, Missouri 63110

(Received 22 November 2005; revised 18 July 2006; accepted for publication 19 July 2006; published 13 September 2006)

In FDG-PET imaging of thoracic tumors, blurring due to breathing motion often significantly degrades the quality of the observed image, which then obscures the tumor boundary. We demonstrate a deblurring technique that combines patient-specific motion estimates of tissue trajectories with image deconvolution techniques, thereby partially eliminating breathing-motion induced artifacts. Two data sets were used to evaluate the methodology including mobile phantoms and clinical images. The clinical images consist of PET/CT co-registered images of patients diagnosed with lung cancer. A breathing motion model was used to locally estimate the location-dependent tissue location probability function (TLP) due to breathing. The deconvolution process is carried by an expectation-maximization (EM) iterative algorithm using the motion-based TLP. Several methods were used to improve the robustness of the deblurring process by mitigating noise amplification and compensating for motion estimate uncertainties. The mobile phantom study with controlled settings demonstrated significant reduction in underestimation error of concentration in high activity case without significant superiority between the different applied methods. In case of medium activity concentration (moderate noise levels), less improvement was reported (10%–15% reduction in underestimation error relative to 15%–20% reduction in high concentration). Residual denoising using wavelets offered the best performance for this case. In the clinical data case, the image spatial resolution was significantly improved, especially in the direction of greatest motion (cranio-caudal). The EM algorithm converged within 15 and 5 iterations in the large and small tumor cases, respectively. A compromise between a figure-of-merit and entropy minimization was suggested as a stopping criterion. Regularization techniques such as wavelets and Bayesian methods provided further refinement by suppressing noise amplification. Our initial results show that the proposed method provides a feasible framework for improving PET thoracic images, without the need for gated/4-D PET imaging, when 4-D CT is available to estimate tumor motion. [DOI: 10.1118/1.2336500]

Key words: breathing motion, positron emission tomography, deconvolution

I. INTRODUCTION

Recent years have witnessed increased use of positron emission tomography (PET), specifically with ^{18}F-FDG (fluoro-2-deoxy-*d*-glucose) molecule which is a marker for increased glycolysis. FDG-PET has been used to provide target volume estimation in different cancer sites such as lung cancer,[1] head and neck cancer,[2] cervical cancer,[3] colorectal cancer,[4] lymphoma,[5] and breast cancer.[6] Studies have demonstrated that the physiological information of PET combined with anatomical structures in CT can improve target volume accuracy in radiotherapy treatment planning.[1] Nevertheless, there are several challenges that are impeding the growing use of PET in treatment planning. PET images inherently suffer from a low spatial resolution due to limited detector efficiency and positron range effects.[7] Physical limitations also include noncollinearity of annihilated gamma rays and uncertainty of their interaction location in the detector's crystals.[8] Other sources of error are caused by the selected reconstruction algorithm because of the tomographic nature of PET acquisition,[9] where such algorithms compromise resolution for reduced image variance.[10] Typically, reconstruction software provide means to correct for radiation attenuation by tissue and photon scattering but not for degradations in spatial resolution.[11] This low resolution results in a partial volume effect in acquired PET images, where the radioactivity concentration is smeared from one area to adjacent areas (spill-in or spill-out).[12] Correction algorithms for partial volume effect have been widely proposed in the literature.[12–15] However, the most prevalent blurring artifact in thoracic PET images is caused by breathing motion.[16,17] Blur due to breathing motion would reduce average uptake measurements up to 30%[16,18] and could decrease detection sensitivity noticeably, in particular for small lesions (less than 15 mm in size) and those lesions close to the diaphragm.[16,19] On the other hand, in PET/CT systems, the data sets are acquired off the gantry are intrinsically aligned: however, the CT data are typically collected within a single breath-hold while the acquisition of PET could take between 20 and 30 min, hence the final PET image is an aggregation over multiple breathing cycles. Such difference in breathing patterns would cause noticeable misregistration error and consequently visible cold spots artifacts near the lung-

diaphragm area if CT is used for attenuation correction of PET.[17,20] Beside the typical errors in locating peripheral and basal lung structures, it is possible for objects below the diaphragm (e.g., liver lesions) to appear in the lung base.[21]

Most treatment planning systems use CT images to contour tumor volume and organ at risk structures. Therefore, several methods have been proposed in literature to reduce breathing artifacts during imaging and radiotherapy treatments. Examples include voluntary or forced breath holding,[22–27] tumor tracking,[28,29] and using external signal with helical 4D CT[30] or spirometry with multislice 4D CT.[31–33] A review of 4D CT methods and their role in treatment planning could be found in Keall.[34] Although PET/CT systems reduce the complexity of registering 4D CT scans with 4D PET scans, the image sets must be temporarily registered as they are not acquired at the same time.

Recently, Nehmeh *et al.*[35] and Low *et al.*[36] have reported the variability of estimating a lesion's activity due to breathing motion in 4D PET/CT. Acquisition in 4D PET could be based on respiratory-phase binning. This could be done either by acquiring positron events only during a gated fraction of the breathing cycle, or by binning according to the breathing phase.[18,35,37–39] Gating could improve the quantification and the resolution of PET images. However, it requires obtaining sufficient scans and may require matching with CT data in each gated phase or bin, which would make the acquisition time too long.[40,41] Nevertheless, in gating techniques, the quality of the resulting images still depends on the synchronization accuracy of the scanned data with the respiratory cycle. This can result in motion artifacts if the window size is too large.

Other suggested techniques require patients to hold breath at mid-expiration or mid-inspiration, or acquire CT during shallow breathing.[17] It is questionable that simple averaging or shallow breathing match blurring effect in PET due to the complex nature of respiratory motion and its heterogeneous influence on different tissues or organs. On the other hand, artifacts will be produced if the patient failed to hold their breath as instructed, which is typically the case in lung cancer patients. To alleviate these problems, techniques that focus on incorporating motion maps directly to correct for breathing artifacts have been proposed. This is done by using 4D-CT motion estimates either to warp the 4D-PET data into the same phase[36,42] or to adjust the reconstruction algorithm by combining all the projection data acquired at the different phases.[43]

In this work, we demonstrate a new deblurring approach that combines patient-specific motion estimates with image deconvolution techniques to compensate for motion induced artifacts in PET images. The proposed technique is currently applied in the image spatial domain to compensate for aggregated target motion artifacts. The reason for selecting the image domain over the sinogram domain is because breathing effects are better understood and motion trajectories are more tractable to model in the image space.

Motion deblurring is viewed in this context as an inverse problem. Deconvolution techniques have been widely applied in optical analysis and video sequence processing to restore the clarity of images.[44–48] They have also been utilized successfully to improve the quality of medical images such as spiral CT acquisition[49] or recently in small animal PET studies,[50] where a Gaussian kernel was used to model scattering. Alternatively, blind deconvolution approaches could be used. This would typically result in a Gaussian-like kernel as well.[51]

In this framework, the imaging system is modeled by[44–48]

$$g(\mathbf{x}) = h(\mathbf{x}) \otimes f(\mathbf{x}) + n(\mathbf{x}), \tag{1}$$

where g is the degraded image; f is the ideal true image; h is a characteristic of the imaging system, typically referred to as the point-spread-function; n is additive noise; $\mathbf{x}$ is the spatial coordinate; and $\otimes$ is the convolution operator. Deblurring or deconvolution in this context is defined as the process of recovering an estimate of $f(\mathbf{x})$ from $g(\mathbf{x})$.

Application of Eq. (1) requires knowledge of the point-spread function or one would need to resort to blind deconvolution techniques as in the spiral CT deblurring example[49] or as in our previous work on static PET deblurring.[51] In this paper, we will only deal with the blurring effect of breathing motion. Hence, we rename the point-spread function the tissue location probability function (TLP). It is important to note that the intrinsic detector resolution and positron range blurring effects could also be included in this deblurring kernel, though we have not done that here. The tissue location probability function is assumed to have finite support size (i.e., it goes to zero within a certain distance), it is positive or zero everywhere, and is shift invariant within the region of interest (the tumor). This last assumption is not a necessity, as deformable image registration methods could be used to form shift-varying TLPs. Often in computer vision applications, a simple motion model is assumed for the TLP, such as uniform velocity or simple harmonic motion.[52] However, the tumor motion due to breathing is more complex. Therefore, in our approach we estimate the breathing motion model directly from 4D CT measurements.[30,31,33,34,53–57] Tidal volume and airflow data measured by spirometry are linearly mapped into spatial trajectories.[58] The model accounts for the observed hysteresis-like behavior of the lung motion.[56] The parameters of the linear model are estimated for each patient case using a template matching algorithm applied to breathing-phase-indexed CT data. The rationale for using CT data for this step is that it provides a motion detection algorithm with distinctive features easier to track than their counterpart in PET. Moreover, 4D CT may often be available in the absence of a true 4D PET implementation.

We use the motion model to locally estimate the TLP.[59] The deconvolution process is carried out via an expectation-maximization (EM) iterative algorithm using the motion-based TLP. In our study, we have investigated various methods to account for noise amplification and uncertainties in the estimated TLP. In addition, we have explored different criteria to assess the EM algorithm convergence as discussed in the following.

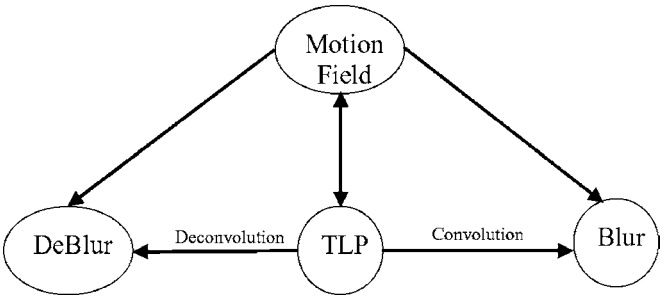

FIG. 1. A block diagram of imaging and convolution/deconvolution interaction. Tissue motion effects can be removed from images via deconvolution, which requires knowledge of the tissue location probability (TLP).

II. MATERIAL AND METHODS

The method was evaluated using an experimental mobile phantom and clinical 4D PET/CT images. The proposed method consists of three steps: (1) motion estimation, (2) conversion of motion estimates into a tissue location probability function (the TLP, which plays the mathematical role of the point spread function in the deconvolution process), and (3) the deconvolution process which is based on the TLP. The block diagram in Fig. 1 sketches the role of convolution/deconvolution in image blurring/deblurring.

A. Data sets

1. Experimental mobile phantom scan

A cylindrical phantom [Fig. 2(a)] was filled with an ^{18}F solution (initial activity of 12 kBq/mL) and three spherical target phantoms of 1.0, 2.0, and 3.0 cm diameter were filled with a ^{11}C solution (initial activity of 170 kBq/mL). Then, a series of 10 min long scans were acquired with estimated activities shown in Fig. 2(b). The phantom was moved under computer control with 1.0 and 2.0 cm amplitudes and alternating each run, resulting in cycles of 2.0 and 4.0 cm motion ranges. The PET scanner was synchronized to 20 acquisition points between the 10 min cycles.

2. Clinical 4D CT and free breathing PET

The data set consisted of PET/CT co-registered images of a patient diagnosed with lung cancer with two lung tumors (Fig. 3): one larger (~80 mm diameter) and one smaller (~19 mm diameter). The PET images have an in-plane spatial resolution of 5.3×5.3 mm/pixel and a slice thickness of 3.4 mm. The CT data have an in-plane spatial resolution of 0.94×0.94 mm/pixel and a slice thickness of 1.5 mm. The tomographic reconstruction was done by ordered-subset expectation-maximization.

B. Estimation of tumor location probability (TLP) function from motion trajectories

The model we used to estimate the motion trajectories was derived from a linear mapping of the tidal volume/airflow space into 3D space at different phases of the breathing cycle.[58] According to this model, the displacement vector ($\vec{\mathbf{x}}_p$) from a reference position at any point of time t could be represented as:[58]

$$\vec{\mathbf{x}}_p(t) = \vec{\mathbf{x}}_v(t) + \vec{\mathbf{x}}_q(t), \tag{2}$$

where $\vec{\mathbf{x}}_v(t)$ and $\vec{\mathbf{x}}_q(t)$ are displacement vectors with magnitudes proportional to the tidal volume ($\alpha * \nu$) and airflow ($\beta * q$). The parameters (α, β) of the model (proportionality constants) were determined by fitting from measured positions using a template matching algorithm, where a template of contoured tumor volume was tracked at different breathing cycle phases. The matching was based on maximizing the normalized cross-correlation between the template and searched regions of the same size in the 4D CT data. The location of the tumor was quantified by its center-of-mass. In Eq. (2), different tumor-location probability functions could be derived, depending on the phase of the breathing cycle under investigation, by changing the reference position.

Next, the tissue trajectories were used to derive the TLP of the tumor motion that caused the blur. This was done by

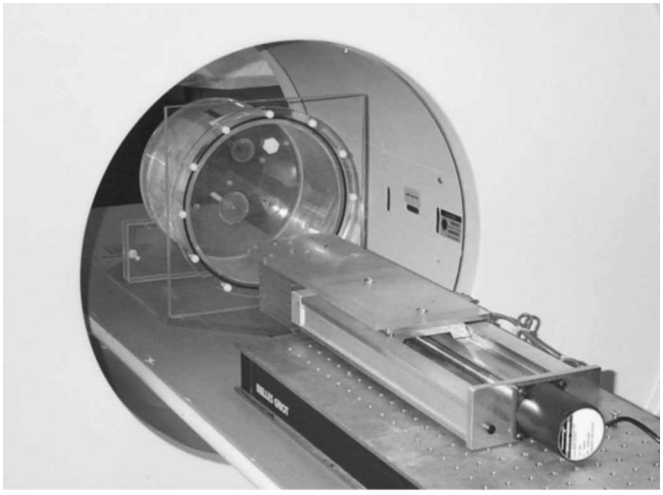

(a)

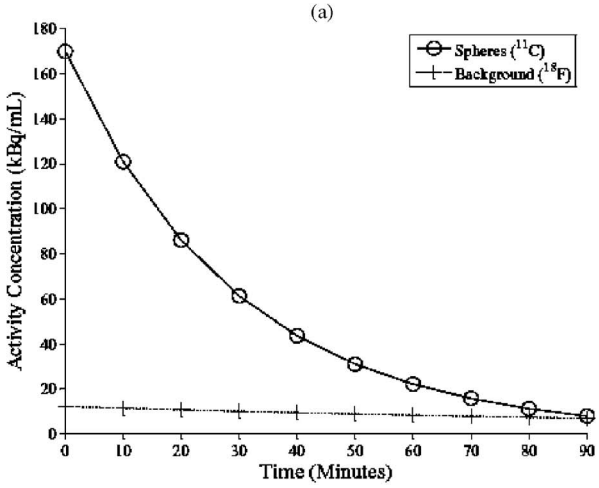

(b)

FIG. 2. Mobile phantom experiment setup. (a) Computer-controlled scanning system and PET phantom with three spheres of diameters 1, 2, and 3 cm. (b) Measured target and background activities at different acquisition times.

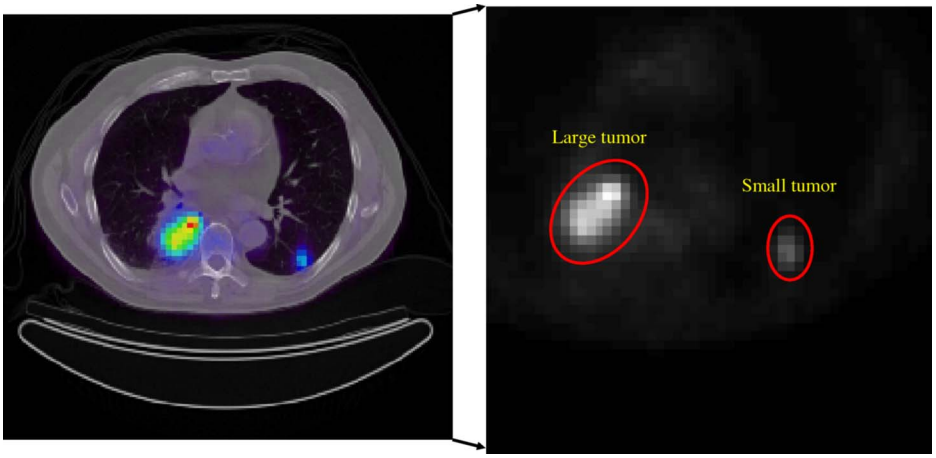

FIG. 3. A patient PET/CT fused image (left) with a large and small tumor enlarged (right).

by tessellating (binning) the 3D probability density function, in which we assume that the intensity at any location (x', y', z') is proportional to the probability (fraction of time) of being at this location. The TLP was then smoothed by spline interpolation and normalized to a total probability of one.[59] It should be emphasized that TLP should be sampled at an appropriate rate, otherwise ringing effect (Gibb's phenomena) artifacts would be observed in the deblurred image.[60] This is particularly true in small lesions, where the TLP was sampled at an increased rate to avoid the ringing and the image was upsampled to the same spatial resolution. After deconvolution process, the image was downsampled back to its original size.

The results for the large and the small tumors' 3D TLP estimates are shown in Figs. 4(c) and 4(d) (as iso-surface images of the 3D probability at different voxel positions from the reference), in Figs. 4(a) and 4(b), we show the 1D histograms in each direction for comparison purposes.

C. Deconvolution

Deconvolution is an inverse filtering process, in which the effects of convolution by a point spread function (TLP in our method) that resulted in the blur are to be inverted.[48] Given the relation in (1), this might sound like a straightforward problem. However, there are several issues that need to be cautiously addressed to achieve a good-quality solution: (1) Motion is generally a spatially varying process, but deconvolution methods generally rely on assuming that the blur is spatially invariant. Therefore, we use a "localized" deconvolution method, over a region small enough to assume that variations in motion are negligible.[46] (2) Direct inversion

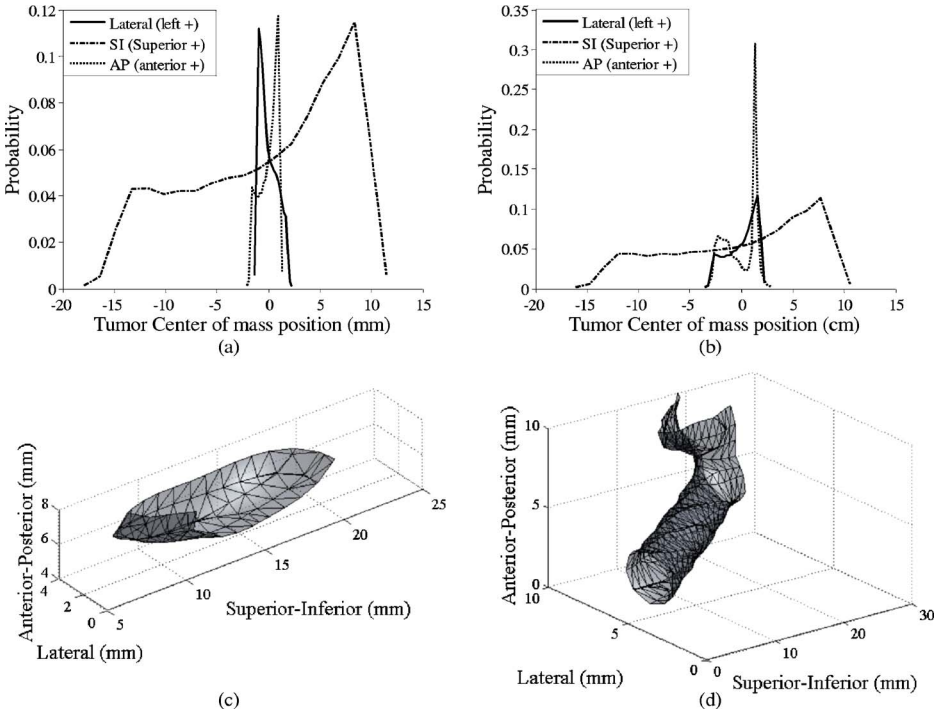

FIG. 4. Histograms of linearly modeled motion in each direction for (a) large tumor and (b) small tumors; (c) and (d) the corresponding estimated 3D TLP rendered surface after tessellation, spline smoothing, and normalization. Note the elongated ellipsoid along the superior-inferior direction. All dimensions are in mm.

using Fourier-based methods would lead to amplification of noise and degradation in the restored image.[47,48] Therefore, several regularized solutions have been proposed in the literature. A frequently used approach is the Wiener filter.[61] However, the regularization parameter and the power spectrum of noise must be estimated. In addition, negative values may appear in the solution. A better alternative is to use methods with non-negativity constraints such as the minimum residual norm with steepest descent, or the expectation maximization method (EM).[45,62] The latter offers a more flexible framework and was used in our study.

The EM-based estimate of the estimated unblurred image f after the kth iteration is given by[62]

$$\hat{f}_{k+1}(\mathbf{x}) = \hat{f}_k(\mathbf{x}) \cdot \left[h(-\mathbf{x}) \otimes \left(\frac{g(\mathbf{x})}{h(\mathbf{x}) \otimes \hat{f}_k(\mathbf{x})} \right) \right], \tag{3}$$

where h is the motion-based TLP, g is the observed image, and the negative sign ($h(-\mathbf{x})$) refers to reflection of the TLP kernel. Multiplication and division are point-by-point within the image. This basic iteration is also known as the Richardson-Lucy iteration and could be derived from the maximum likelihood of a Poisson distribution.

Accurate implementation of (3) requires complete knowledge of the TLP, which is not always available. Sometimes the TLP is partially known or is uncertain. In such cases, methods of "myopic deconvolution" are applied, wherein one accounts for the uncertainty in the TLP (Δh).[63,64] Or, in the extreme case, when the TLP is unknown, so-called "blind deconvolution"[65] is used. The term myopic is used to indicate that the TLP is partially known only. The TLP is estimated by reversing the roles of h and f in (3), alternately iteration between refining the TLP estimate and the unblurred image estimate.[65] Another problem in (3) is the amplification of noise while iterating. Methods based on the wavelet transform have demonstrated excellent results in denoising, beside the other advantages of multiresolution approach and the sparse representation of the wavelet coefficients.[60,66,67] One way of applying wavelet to the deconvolution process is to track a residual error (R) as follows:[60,68]

$$R_k(\mathbf{x}) = g(\mathbf{x}) - h(\mathbf{x}) \otimes \hat{f}_k(\mathbf{x}). \tag{4}$$

Then, by using a translation invariant transform:

$$R_k(\mathbf{x}) = c_j + \sum_{j=1}^{J} W_j(\mathbf{x}), \tag{5}$$

where c_j is the low-pass filtered version at scale j; J is the total number of scales, and the W_j are the wavelet coefficients. Then, the wavelet coefficients are thresholded to extract only the significant structures from the residuals at each iteration $\hat{R}_k$. After the residual is wavelet-denoised, the regularization effect could be incorporated into the algorithm either by a weighted addition to $\hat{f}_k(\mathbf{x})$ to comprise the next iteration (referred to as the Van Cittert's method),[69,70] or by recomputing $g(\mathbf{x})$ from Eq. (4) using $\hat{R}_k$ and applying it in Eq. (3) to yield the next estimate of $\hat{f}$. In this work, we have chosen the second approach because it does not require further trial and error to estimate the weighting factor in Van Cittert's method. In this realm, wavelets suppress noise in a natural way during the deconvolution process, whereas Fourier low-pass filtering has difficulty controlling deconvolution-induced noise. Note that in our implementation, the convolution process was performed in the Fourier domain to achieve high efficiency (even though wavelet hard-threshold denoising is still applied at each iteration).

We used the 9,7-biorthogonal basis functions of the wavelet transform, which are used in the JPEG2000 standard.[71,72] Furthermore, "Spin-cycling," which refers to choosing nine different nearest-neighbor points in the image as computational centers, was used to reduce small artifacts introduced by the wavelet transform.[66] The hard-threshold value is given as percentage of the maximum wavelet's coefficient values. The 2D transform is applied to each 3D image slice. This is a limitation in our implementation, but it is not a trivial task to generalize these basis functions to fully 3D.

We also investigated the use of image priors in a Bayesian framework and the effect of TLP uncertainty. In the case of Bayesian deconvolution, a Poisson maximum *a posteriori* estimate would yield the following iteration:

$$\hat{f}_{k+1}(\mathbf{x}) = \hat{f}_k(\mathbf{x}) \cdot \exp\left[\left(\frac{g(\mathbf{x})}{h(\mathbf{x}) \otimes \hat{f}_k(\mathbf{x})} - 1 \right) \otimes h(-\mathbf{x}) \right]. \tag{6}$$

The exponential term in this case would enforce the positivity constraint and regularize the solution.

In order to account for uncertainty, a myopic method was used, where the initial estimate (guess) was set to the known TLP, and the double-alternating iterative method was used to simultaneously update the TLP and deconvolve the image.

III. EXPERIMENTAL RESULTS

A. Application to mobile phantom scan

We conducted experiments using a mobile phantom scan at different activity concentration levels [see Fig. 2(b)] and different ranges of motion (2 and 4 cm). The activities were divided into three categories: (1) High activity (greater than 80 kBq/mL), (2) medium activity (between 30 and 80 kBq/mL), (3) low activity (less than 30 kBq/mL). Each category had cases of short motion range (2 cm) and long motion range (4 cm) with estimated 1D TLP shown in Fig. 5. The average activity concentration in each sphere was measured within the region-of-interest (ROI) since the sphere is of known location and diameter using the phantom at rest (static phantom as a reference), sample images of the static reference sphere images at different concentration are shown in Fig. 6. Motion simulated images are shown in Fig. 7. Note the resulting "hotdog" like images. Quantitatively, motion blur results in underestimation of the PET activity concentration. In Fig. 8, we summarize the results of applying the different deconvolution algorithms and we show the resulting error after applying each method. The parameters for each of the methods have been fixed throughout the experi-

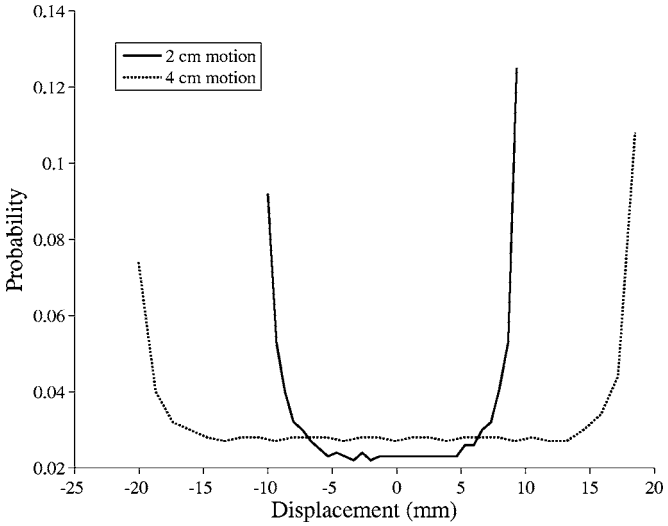

FIG. 5. Estimated TLP of mobile phantom with motion ranges of 2 and 4 cm.

ments to provide a *baseline* comparison. For each method, the parameters are optimized so that over-deblurring and noise amplification are minimized. For basic EM deconvolution [Eq. (3)], the number of iterations was set to 3, as well as for blind and myopic deconvolution. In case of Bayesian deconvolution the number of iterations was set to 5 and in case of wavelet deconvolution, the number of iterations was also 5, and the threshold is 10%. Regularized algorithms can tolerate larger number of iterations without generating artifacts. In the case of high activity concentration [Figs. 8(a) and 8(b)], the different deconvolution methods resulted in 15%–20% reduction of underestimation error. Moreover, in shorter motion case [Fig. 8(b)] the error is almost within ±5% for 2- and 3-cm-diam spheres. The larger the motion the more residual error would remain. Note that in practical situations further improvement could be achieved by increasing the number of iterations for each case (see Fig. 9). The best performance was obtained by the Bayesian and the wavelet methods, but the improvement was subtle over basic EM. However, in case of medium concentration the wavelet method provided significant improvements over other techniques. But in the case of low activity, none of the methods provided substantial improvement except in the case of small motion and large sphere [Fig. 8(f)], where the error was less than 2%, though over-deblurring is noticed. Sample results of applying the different deconvolution methods to the medium concentration case with 2 cm motion are presented in Fig. 10.

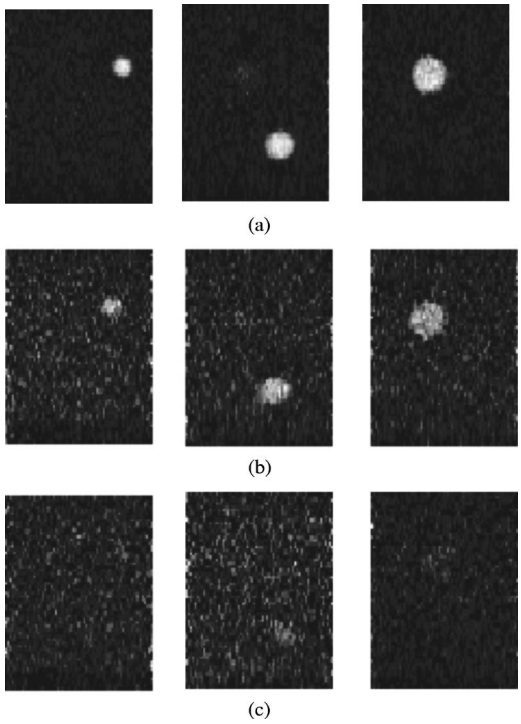

FIG. 6. Phantom static (at rest) reference images in coronal view with 1, 2, and 3 cm spheres diameters (left to right). (a) At high activity concentration (low noise) of 4 cm motion, (b) medium activity concentration (moderate noise) of 2 cm motion, (c) low activity concentration (very high noise) of 4 cm motion range.

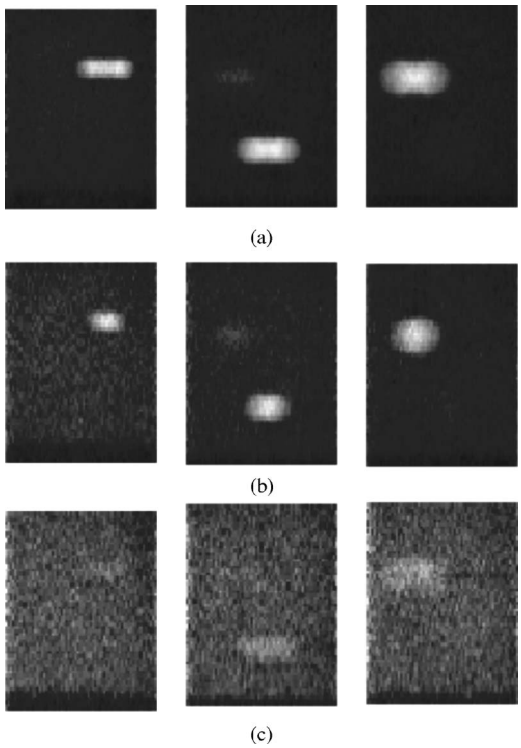

FIG. 7. Motion simulated phantom image in coronal view with 1, 2, and 3 cm spheres diameters (left to right). (a) At high activity concentration (low noise) of 4 cm motion, (b) medium activity concentration (moderate noise) of 2 cm motion, (c) low activity concentration (very high noise) of 4 cm motion range. Note the "hotdog" shape due to motion (a) and (c) of 4 cm and (b) of 2 cm. Moreover, blurring has the advantage of "smoothing" the noise, however, distorting the shape. So, a chosen deconvolution method should restore the shape without amplifying the noise.

B. Application to clinical PET data

We also evaluated the proposed motion-based deblurring algorithm on a co-registered patient PET/CT data set, containing two lung tumors, one much larger than the other, as

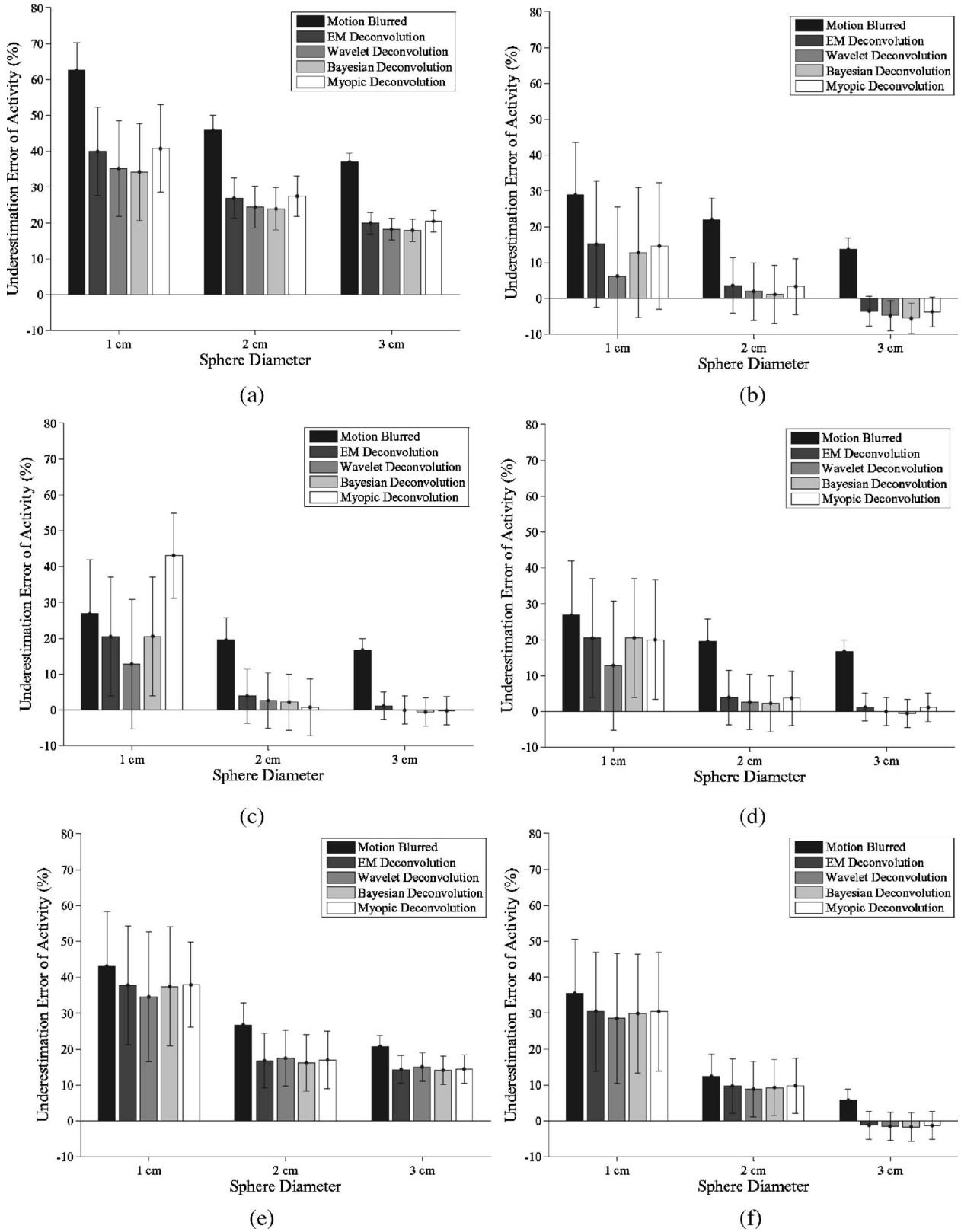

FIG. 8. Evaluation analysis of mobile phantom experiments showing percentage of activity concentration underestimation error with different methods. The error bars represent one standard error of voxel intensity deviation within the region-of-interest. (a) High activity concentration (low noise) with 4 cm range of motion, (b) high activity concentration (low noise) with 2 cm range of motion, (c) medium activity concentration (moderate noise) with 4 cm range of motion, (d) medium activity concentration (moderate noise) with 2 cm range of motion, (e) low activity concentration (high noise) with 4 cm range of motion, (f) low activity concentration (high noise) with 2 cm range of motion.

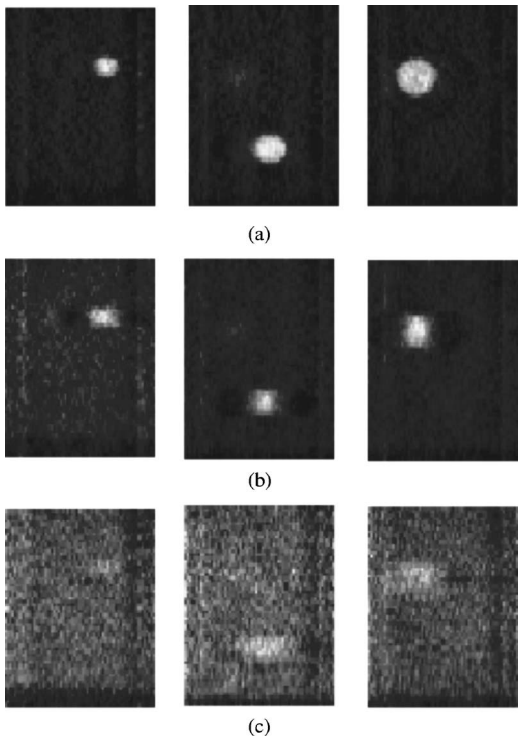

FIG. 9. EM deconvolved phantom image in coronal view with 1, 2, and 3 cm spheres diameters (left to right). (a) At high activity concentration (low noise) of 4 cm motion (10 EM iterations), (b) medium activity concentration (moderate noise) of 2 cm motion (5 EM) iterations, (c) low activity concentration (very high noise) of 4 cm motion range (3 EM iterations).

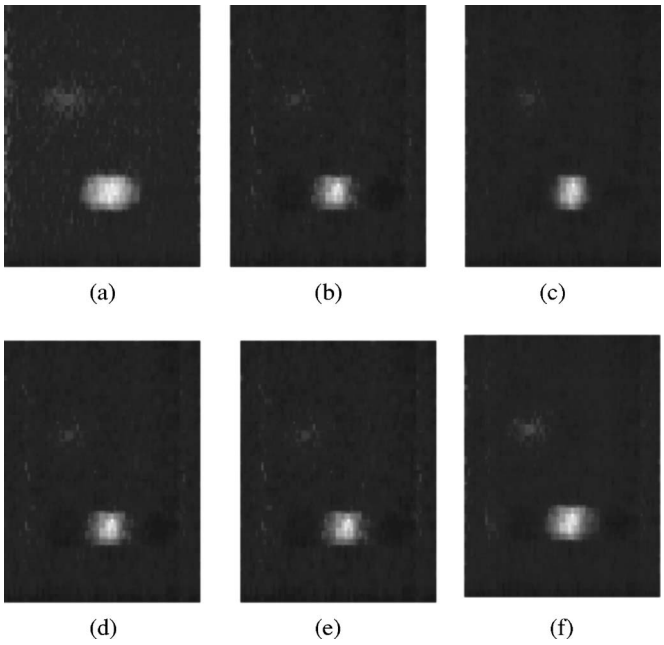

FIG. 10. A comparison of the different deconvolution methods applied to medium activity sphere of 2 cm diameter and 2 cm range of motion. (a) Original coronal view; (b) EM deblurred with 5 iterations; (c) blind deconvolution with 5 iterations; (d) myopic deconvolution with 5 iterations; (e) Bayesian deconvolution with 10 iterations; (f) wavelet-based deconvolution with a threshold of 10% and after 10 iterations.

shown in Fig. 3. In the absence of a "true image" as a benchmark, we used the following metrics for quantitative evaluation of the deblurred PET data.

1. A figure-of-merit (FOM): this metric is frequently used in the deconvolution literature, and is defined as the mean-squared-difference between the blurred and the estimated deblurred image after convolution with the TLP (reblurred).

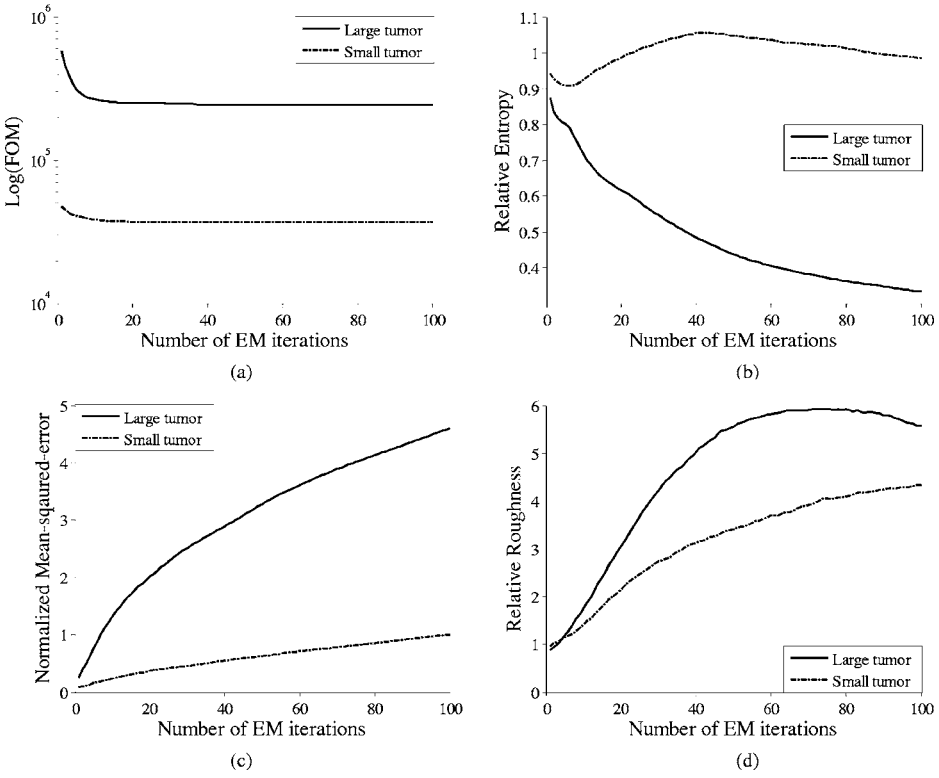

FIG. 11. Quantitative analysis of EM deconvolution for clinical PET data. (a) Figure-of-merit (FOM) vs the number of the EM iterations for the large and the small lung tumors. The deconvolution converged within 15 iterations in both cases; (b) entropy vs number of iterations; (c) normalized mean-squared-error (NMSE) vs number of iterations; (d) roughness vs number of iterations. Note from the entropy graph, the minima achieved in the case of the small tumor around 5 iterations. This suggests early stopping of EM iterations.

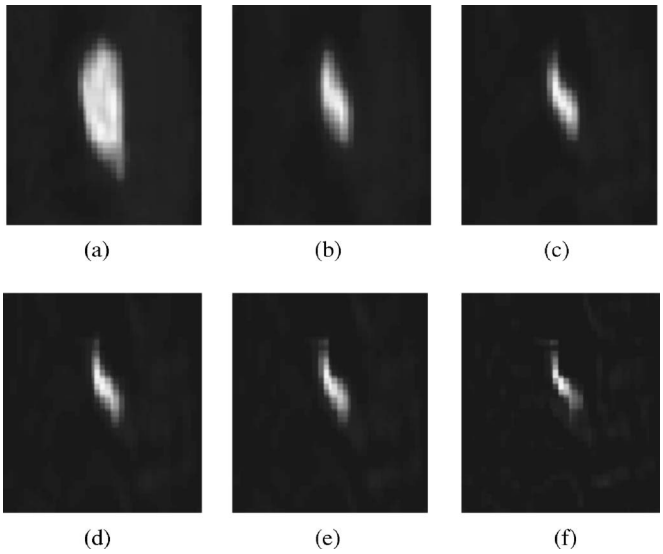

FIG. 12. Deconvolution results for the large tumor using a different number of EM iterations. (a) original coronal view (direction of largest motion) for the large tumor; (b) after 5 iterations; (c) after 10 iterations; (d) after 15 iterations (converged according to FOM); (e) after 20 iterations; and (f) after 50 iterations. Note the presence of visible artifacts in this case.

2. Shannon's entropy: This is a measure of uncertainty. Deblurring is a process of recovering the signal, i.e., increasing our information (minimizing entropy). For instance, an impulse signal after blurring tends to spread out. The metric is given by

$$\text{entropy ratio} = \frac{E_d}{E_p}, \tag{7}$$

where E_d is the entropy of the deconvolved image, E_p is the entropy of the original PET image. Entropy is defined as $E = \sum_{i=1}^{N} p_i \ln(p_i)$, where p is estimated from the image histogram with N bins.

3. Normalized mean squared error (NMSE): defined as the variance of the difference between the blurred and deblurred images scaled by the blurred variance. This is a common metric in restoration problems and in this case it provides a measure of the aggressiveness of deblurring. This metric essentially just monitors the difference between the deblurred image and the original blurred image.

4. Roughness: is defined as the square root of the median of the squared Laplacian (second-order derivative of the local image intensity region). The median operator makes the metric nearly independent of small regions or large values (near sharp edges or corners).[66] This metric monitors the aggressiveness of the deconvolution. At early stages it increases due to deblurring/sharpening; in later iterations roughness increases further due to deconvolution noise amplification.

The figure-of-merit measures convergence for an ideal TLP, but this may not be possible in practical situations where our knowledge of the TLP is incomplete due to uncertainties in motion estimation, noise amplification, and other undetermined factors that could contribute to the blurriness. Hence, "early stopping" rules become necessary.

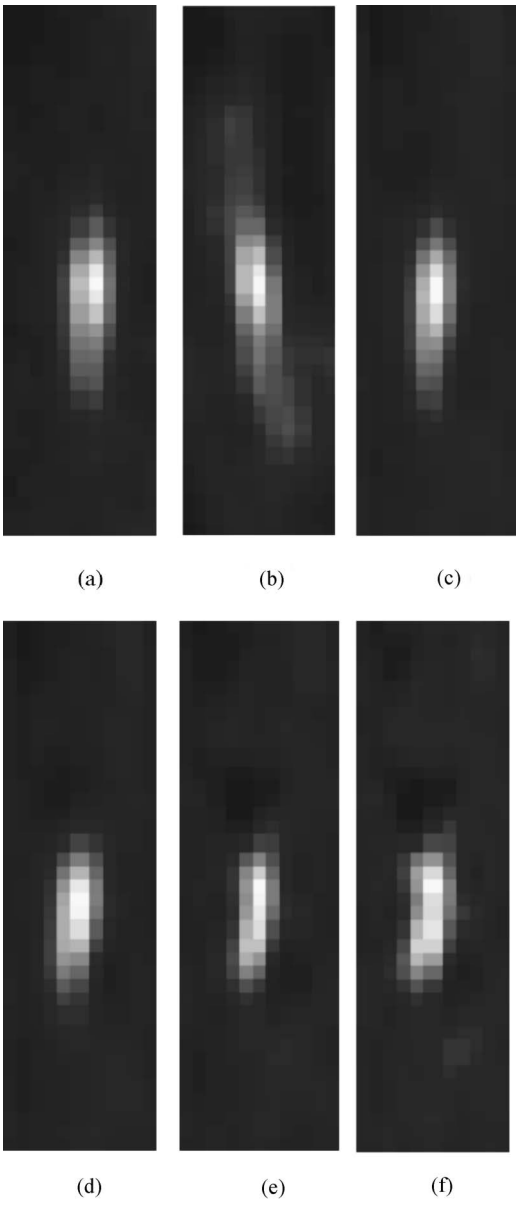

FIG. 13. Deconvolution results for the small tumor. (a) Original coronal view; (b) deblurring without accounting for limited support size. Note the ringing effects. The EM results after resampling correction. (c) After 2 iterations; (d) after 5 iterations (early stopping is recommended according to entropy); (e) after 10 iterations; (f) after 15 iterations (converged according to FOM, but notice the noise artifacts); and (g) after 20 iterations.

In Fig. 4, we show histograms of the motions in each direction and the estimated 3D TLP for both tumors. Evaluation using the metrics is shown in Fig. 11. For the larger tumor, following the guidance of FOM [Fig. 11(a)], the metric indicates convergence of the deconvolution process around 15 iterations (range from 10 to 20); the other metrics did not support early stopping. However, in the case of the smaller tumor, FOM again shows convergence of the deconvolution process around 15 iterations (range from 10 to 20), but the entropy metric [Fig. 11(b)] shows a minimum at

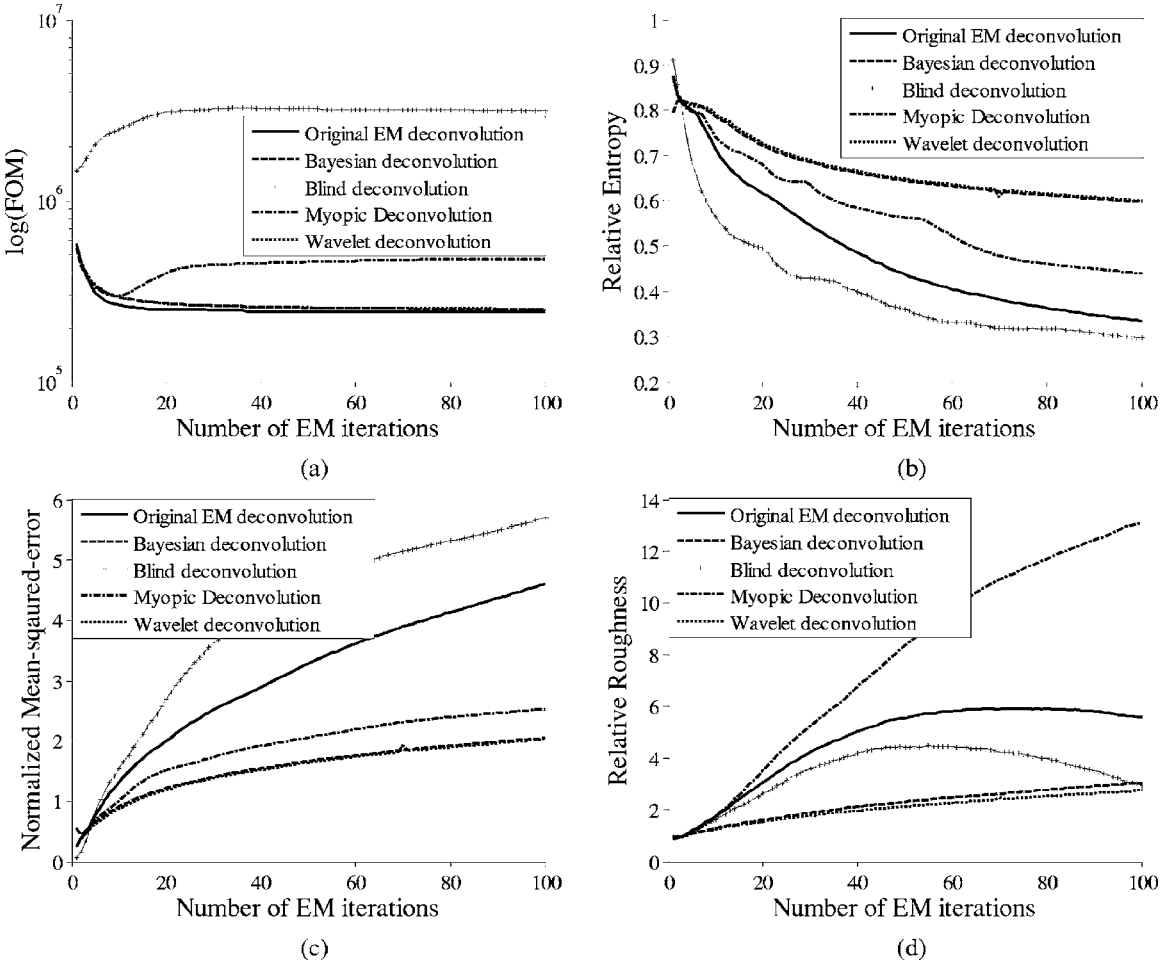

FIG. 14. A quantitative comparison of the different deconvolution methods applied to the large tumor. (a) FOM vs number of iterations, note the overshoot in the blind deconvolution and the variation in myopic deconvolution after 10 iterations; (b) entropy vs number of iterations, where the blind deconvolution tends to over-deblur the image with a Gaussian-type PSF; (c) NMSE vs number of iterations; and (d) roughness vs number of iterations. The wavelet-based (threshold = 1%) and the Bayesian deconvolution yielded comparable performances (the curves are quite close to each other relative to the other methods).

around 5–6 iterations, after which the entropy increases. This suggests that noise amplification is overtaking the deblurring process causing an increase of entropy. Hence, this indicates a termination point. Such trends are also observed in Figs. 12 and 13.

In Figs. 12 and 13 we show results in the coronal view since most of the effect takes place in the cranio-caudal direction. Moreover, in Fig. 13 we also show the ringing effect in case of the small tumor eliminated by sampling the TLP at a higher rate.

C. Modifications to the deconvolution method

We incorporated wavelet denoising into the deconvolution process to mitigate the effect of noise amplification. We also experimented with using Bayesian priors and myopic deconvolution (partially known TLP) and the extreme case of no knowledge to simulate uncertainties in TLP.

In Figs. 14 and 15, we show the estimates of the different quantitative metrics for the large and small tumor and in Figs. 16 and 17 we provide a representative sample of results.

It is seen in Figs. 14(a), 15(a), 16(c), and 17(c) that blind deconvolution did not converge. We initially estimated the TLP to be constant with a support size equal to the motion estimated TLP. The myopic deconvolution was stopped early at 10 iterations. The wavelet-based deconvolution and the Bayesian approach yielded similar performances. Similar conclusions could be deduced from the entropy results in Figs. 14(b) and 15(b). However, blind deconvolution had a relatively faster reduction in entropy as there is no distinction in the algorithm between the motion deblurring and other residual deblurring.

Compared to the EM methods, wavelet-based deconvolution with an empirical threshold value of 1% resulted in the most visually appealing images, and seems promising for further research [see Figs. 16(f) and 17(f)]. This is due to the fact that the original EM method is not immune to noise amplification.

IV. DISCUSSION

The aim of this study was to investigate new deconvolution methods for respiratory motion compensation in thoracic

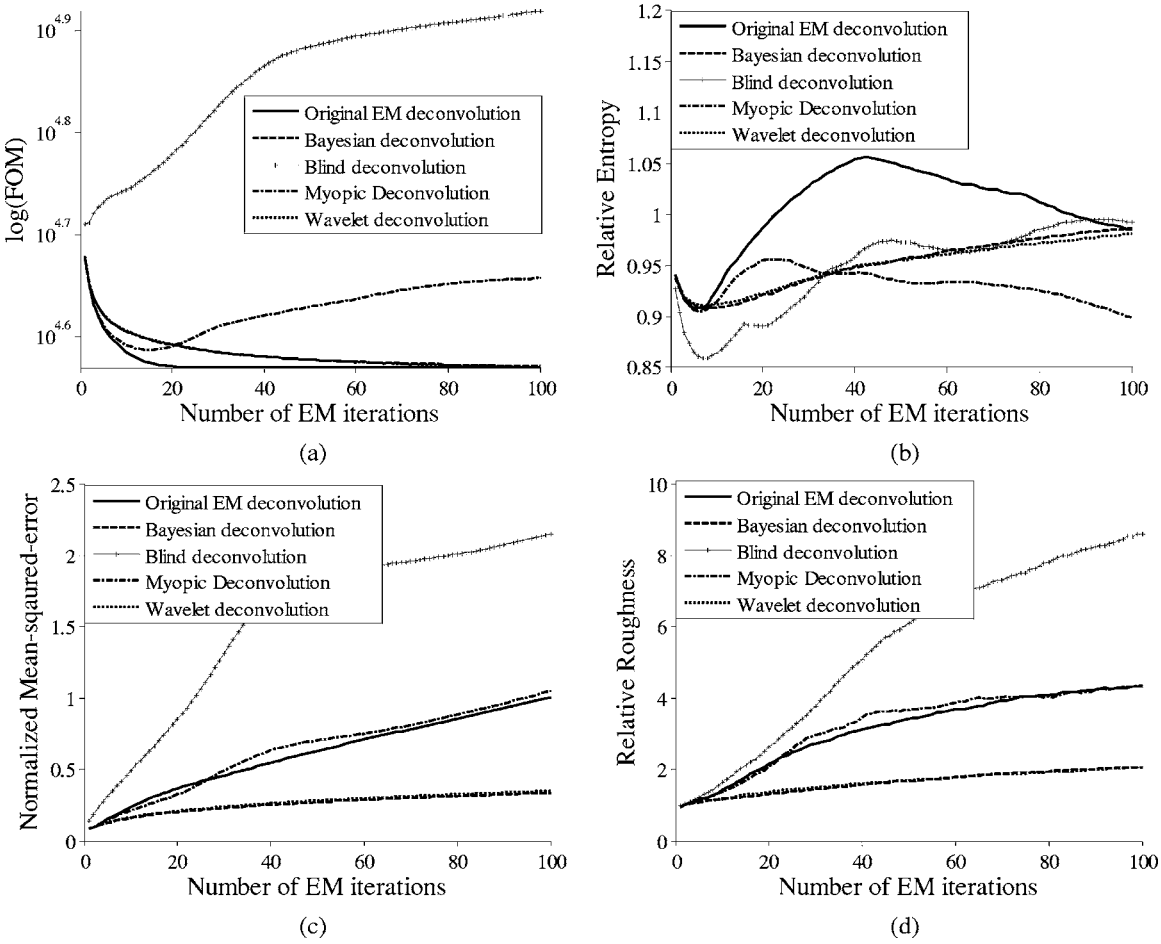

FIG. 15. A quantitative comparison of the different deconvolution methods applied to the small tumor. (a) FOM vs number of iterations, note again the overshoot in the blind deconvolution; (b) entropy vs number of iterations, where the blind deconvolution tends to over-deblurr the image with a Gaussian-type PSF. In this case, entropy suggests an early stopping of 5–6 iterations; (c) NMSE vs number of iterations; and (d) roughness vs number of iterations. The wavelet-based (threshold = 1%) and the Bayesian deconvolution yielded close performances (the curves are quite close to each other relative to the other methods).

PET images. We believe that deconvolution could be used as a postprocessing tool to mitigate the blurring artifacts of breathing motion and could be used as an alternative for externally triggered gating and other binning techniques. However, deblurring is an ill-posed inverse problem with no unique optimal solution. Therefore, in our investigation we noticed that the following requirements need to be carefully considered in order to successfully apply deconvolution for deblurring of motion artifacts in PET images. First, an accurate estimation of the motion trajectory is required, which can be obtained from 4D CT. The patient-specific model plays a vital role in shaping the deblurring results. In our case, we used a recently developed breathing motion model[58] that maps measured patient's tidal volume and airflow to spatial positions in the image domain. Hence, it is important to note that the probability density function we used is confined to positional blurring only (the TLP) rather than including other factors related to image system blurring. Combining the TLP kernel with an image system blurring kernel would potentially be advantageous. We attempted to account for uncertainty in the estimated TLP by using a "myopic" approach (assuming partially known blur); however, our

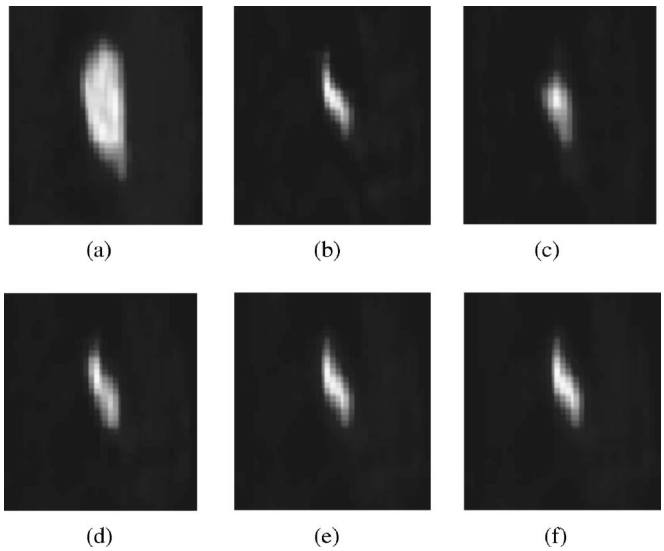

FIG. 16. A comparison of the different deconvolution methods applied to the large tumor. (a) Original coronal view; (b) EM deblurred with 15 iterations; (c) blind deconvolution with 10 iterations; (d) myopic deconvolution with 10 iterations; (e) Bayesian deconvolution with 15 iterations; (f) wavelet-based deconvolution with a threshold of 1% and after 15 iterations.

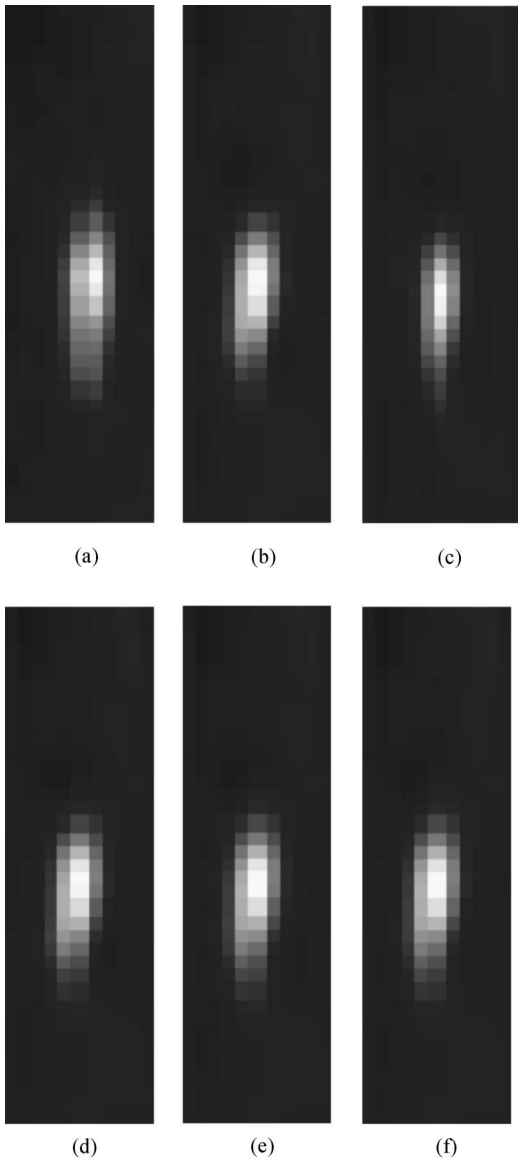

FIG. 17. A comparison of the different deconvolution methods applied to the small tumor. (a) Original coronal view; (b) EM deblurred with 5 iterations; (c) blind deconvolution with 5 iterations; (d) myopic deconvolution with 5 iterations; (e) Bayesian deconvolution with 5 iterations; (f) wavelet-based deconvolution with threshold of 1% and after 5 iterations.

simulations showed this to be of limited advantage, possibly due to the fact the algorithm would stray between different blurring sources, or indicating the need for explicitly including the uncertainty in the point spread function.[73] On the other hand, simulations with blind deconvolution in most cases resulted in artifacts when motion is present. The second consideration is the size of the TLP support relative to the object. If the size of the object is too small this will cause ringing effects, known as Gibbs phenomena. To alleviate this problem in small tumors, we applied deconvolution at a sampling rate higher than the typical voxel size. In this case, the tumor area was up-sampled (by a factor of 5) to a finer grid similar to that of the high rate TLP. We then performed the deconvolution on this finer grid, and down-sampled the results to the original size. This process introduces blurring due to interpolation, but this could be partially eliminated by increasing the number of iterations in the EM algorithm. A third issue is that deconvolution is "valid" only within its region of interest. If no shift-varying techniques are employed, the algorithm may well generate undesirable artifacts. Finally, to resolve the dilemma of sharpening versus noise amplification that is prevalent in deconvolution, we have investigated two regularization methods: wavelet denoising of residuals after each iteration, or using Bayesian priors. Both methods seemed to reduce the noise degradation, especially in the case of wavelet, which provided overall the best performance. Other wavelet-based methods could be applied with direct extension to 3D and employment of shrinkage methods for automated selection of the threshold value, which may offer better solutions.[74] Moreover, other denoising methods[75] such as anisotropic diffusion could be investigated as well. By the same token, the Bayesian approach could be further enhanced by deriving more informed priors.

Applying the explored deconvolution methods to the different data sets demonstrated underestimation error reduction by about 10%–20% using the wavelet method. The improvement is noticed to be better when the object size is larger and the motion range is smaller. This could be attributed to the interplay among ringing effects, noise amplification, and number of iterations on the convergence of the EM algorithm. At low noise level (high activity concentration), the methods provided similar performances with an average reduction of underestimation error of 15%–20%. At medium noise level (medium activity concentration), the wavelet offered the best correction. At high noise (low activity concentration), none of the methods seem to offer improvement for the small object and modest improvements were observed for the larger objects. In case of real clinical data, where no truth is known, we investigated several metrics to quantify the selection of the deconvolution parameters, specifically the number of EM iterations. Our simulations suggest that a good criterion would be to compromise between convergence as indicated by the figure-of-merit and increase of entropy, which indicates noise amplification.

A main limitation of the deconvolution methods is that they work on the aggregated image and not on phase by phase basis. However, this means that no breathing-phase tracking is required during acquisition, hence, less computational burden and discomfort to the patient. Previously published methods to address PET breathing motion effects have focused on correcting acquired events in list mode and rebinning the sinogram data before reconstruction,[76] but such methods suffer from missing data artifacts. This could be alleviated for simple uniform motion patterns;[77] however, in the case of complex respiratory motion this could be a challenging task and a possible direction for future work.

V. CONCLUSIONS

We have introduced the concept of deblurring time-averaged PET images to control for the effect of breathing

motion. The method may be a simpler and less time consuming alternative to requiring breathing monitoring and fully 4D event-binning, reconstruction, and re-registration (i.e., registering images taken at varying breathing phases).[19,30,35,39,40,53] Several deconvolution methods have been examined, including methods which require little information about the breathing pattern motion of the tumor (only partially successful) to more accurate methods which require approximate tumor trajectories during breathing. The initial results show that the method is promising for either large or small tumors. Our results indicate that using the wavelet-based techniques and Bayesian estimation provided the best performance for motion deblurring. Issues to be further investigated to fully establish and validate the proposed method for clinical use include testing on more clinical data sets and robustness to uncertainties in the motion model derived from the corresponding 4D CT scan.

[a]Electronic mail: elnaqa@wustl.edu

[1]J. Bradley *et al.*, "Impact of FDG-PET on radiation therapy volume delineation in non-small-cell lung cancer," Int. J. Radiat. Oncol., Biol., Phys. **59**, 78–86 (2004).
[2]J. P. Suarez Fernandez *et al.*, "Positron emission tomography (PET) imaging in head and neck cancer," Acta Otorrinolaringol Esp. **55**, 303–309 (2004).
[3]S. Mutic *et al.*, "PET-guided IMRT for cervical carcinoma with positive para-aortic lymph nodes—a dose-escalation treatment planning study," Int. J. Radiat. Oncol., Biol., Phys. **55**, 28–35 (2003).
[4]F. Y. Liu *et al.*, "Utility of 2-fluoro-2-deoxy-D-glucose positron emission tomography in managing patients of colorectal cancer with unexplained carcinoembryonic antigen elevation at different levels," Dis. Colon Rectum (2005).
[5]P. Castellucci *et al.*, "18F-FDG PET early after radiotherapy in lymphoma patients," Cancer Biother. Radiopharm. **19**, 606–612 (2004).
[6]H. J. Biersack, H. Bender, and H. Palmedo, "FDG-PET in monitoring therapy of breast cancer," Eur. J. Nucl. Med. Mol. Imaging **31**, S112–117 (2004).
[7]E. J. Hoffman *et al.*, "Quantitation in positron emission computed tomography. 6. Effect of nonuniform resolution," J. Comput. Assist. Tomogr. **6**, 987–999 (1982).
[8]T. Lewellen and J. Karp, "PET Systems," in *Emission Tomography: The Fundamentals of PET and SPECT*, edited by M. Wernick and J. Aarsvold (Elsevier, Amsterdam, 2004), pp. 179–194.
[9]D. Lalush and M. N. Wernick, "Iterative image reconstruction," in Ref. 8, pp. 443–472.
[10]J. M. Ollinger and J. A. Fessler, "Positron emission tomography," IEEE Signal Process. Mag. **14**, 43–55 (1997).
[11]E. D. Morris *et al.*, "Kinetic modeling in positron emission tomography," in Ref. 8, pp. 499–540.
[12]D. Strul and B. Bendriem, "Robustness of anatomically guided pixel-by-pixel algorithms for partial volume effect correction in positron emission tomography," J. Cereb. Blood Flow Metab. **19**, 547–559 (1999).
[13]O. Rousset, Y. Ma, and A. Evans, "Correction for partial volume effects in PET: Principle and validation," J. Nucl. Med. **39**, 904–911 (1998).
[14]C. H. Chen *et al.*, "Simultaneous recovery of size and radioactivity concentration of small spheroids with PET data," J. Nucl. Med. **40**, 118–130 (1999).
[15]R. F. Muzic, Jr., C. H. Chen, and A. D. Nelson, "A method to correct for scatter, spillover, partial volume effects in region of interest analysis in PET," IEEE Trans. Med. Imaging **17**, 202–213 (1998).
[16]L. Boucher *et al.*, "Respiratory Gating for 3-dimensional PET of the thorax: Feasibility and initial results," J. Nucl. Med. **45**, 214–219 (2004).
[17]W. Sureshbabu and O. Mawlawi, "PET/CT imaging artifacts," J. Nucl. Med. Technol. **33**, 156–161 (2005).
[18]S. A. Nehmeh *et al.*, "Effect of respiratory gating on quantifying PET images of lung cancer," J. Nucl. Med. **43**, 876–881 (2002).
[19]Z. Zhu, B. M. W. Tsui, and W. P. Segars, "A simulation study of the effect of gating scheme on respiratory motion bluffing in FDG Lung PET," IEEE Nuclear Science Symposium Conference Record 2002, Vol. 3, pp. 1554–1558.
[20]K. Wechalekar, B. Sharma, and G. Cook, "PET/CT in oncology—a major advance," Clin. Radiol. **60**, 1143-1155 (2005).
[21]M. M. Osman *et al.*, "Respiratory motion artifacts on PET emission images obtained using CT attenuation correction on PET-CT," Eur. J. Nucl. Med. Mol. Imaging **30**, 603–606 (2003).
[22]J. W. Wong *et al.*, "The use of active breathing control (ABC) to reduce margin for breathing motion," Int. J. Radiat. Oncol., Biol., Phys. **44**, 911–919 (1999).
[23]D. Mah *et al.*, "Technical aspects of the deep inspiration breath-hold technique in the treatment of thoracic cancer," Int. J. Radiat. Oncol., Biol., Phys. **48**, 1175–185 (2000).
[24]K. E. Rosenzweig *et al.*, "The deep inspiration breath-hold technique in the treatment of inoperable non-small-cell lung cancer," Int. J. Radiat. Oncol., Biol., Phys. **48**, 81–87 (2000).
[25]K. E. Rosenzweig *et al.*, "Tumor motion control in the treatment of non small cell lung cancer," Cancer Invest **23**, 129–133 (2005).
[26]J. Hanley *et al.*, "Deep inspiration breath-hold technique for lung tumors: The potential value of target immobilization and reduced lung density in dose escalation," Int. J. Radiat. Oncol., Biol., Phys. **45**, 603–611 (1999).
[27]T. Tada *et al.*, "Lung cancer: Intermittent irradiation synchronized with respiratory motion—results of a pilot study," Radiology **207**, 779–783 (1998).
[28]H. Shirato *et al.*, "Physical aspects of a real-time tumor-tracking system for gated radiotherapy," Int. J. Radiat. Oncol., Biol., Phys. **48**, 1187–1195 (2000).
[29]H. Shirato *et al.*, "Speed and amplitude of lung tumor motion precisely detected in four-dimensional setup and in real-time tumor-tracking radiotherapy," Int. J. Radiat. Oncol., Biol., Phys. **64**, 1229–1236 (2006).
[30]S. S. Vedam *et al.*, "Acquiring a four-dimensional computed tomography dataset using an external respiratory signal," Phys. Med. Biol. **48**, 45–62 (2003).
[31]D. A. Low *et al.*, "A method for the reconstruction of four-dimensional synchronized CT scans acquired during free breathing," Med. Phys. **30**, 1254–1263 (2003).
[32]I. El Naqa *et al.*, "Automated 4-D lung computed tomography reconstruction during free breathing for conformal radiation therapy," In: *Medical Imaging*, edited by A. Amini and A. Manduca, Vol. 5369, (SPIE, San Diego, 2004), pp. 100–106.
[33]W. Lu *et al.*, "Quantitation of the reconstruction quality of a four-dimensional computed tomography process for lung cancer patients," Med. Phys. **32**, 890–901 (2005).
[34]P. Keall, "4-dimensional computed tomography imaging and treatment planning," Semin. Radiat. Oncol. **14**, 81–90 (2004).
[35]S. A. Nehmeh *et al.*, "Four-dimensional (4D) PET/CT imaging of the thorax," Med. Phys. **31**, 3179–3186 (2004).
[36]D. Low *et al.*, *A method for acquiring PET images without breathing motion artifacts*, AAPM, Vol. 32 (Medical Physics, Seatle, 2005), pp. 2095–2096.
[37]S. M. Larson *et al.*, "PET/CT in non-small-cell lung cancer: value of respiratory-gated PET, "Chang Keng I Hsueh **28**, 306–314 (2005).
[38]S. A. Nehmeh *et al.*, "Quantitation of respiratory motion during 4D-PET/CT acquisition," Med. Phys. **31**, 1333–1338 (2004).
[39]S. A. Nehmeh *et al.*, "Reduction of respiratory motion artifacts in PET imaging of lung cancer by respiratory correlated dynamic PET: methodology and comparison with respiratory gated PET," J. Nucl. Med. **44**, 1644–1648 (2003).
[40]Y. Wang *et al.*, "A simple respiration gating technique and its application in high-resolution PET camera," IEEE Trans. Nucl. Sci. **52**, 125–129 (2005).
[41]T. Pan *et al.*, Attenuation correction of PET images with respiration-averaged CT images in PET/CT, J. Nucl. Med. **46**, 1481–1487 (2005).
[42]T. Zhang *et al.*, "Deformable fusion of 4D-PET images (Abstract) AAPM," Med. Phys. **32**, 2082 (2005).
[43]T. Li *et al.*, "Model-based image reconstruction for four-dimensional PET," Med. Phys. **33**, 1288–1298 (2006).
[44]A. K. Jain, *Fundamentals of Digital Image Processing* (Prentice Hall, Englewood Cliffs, NJ, 1989).
[45]C. R. Vogel, *Computational Methods for Inverse Problems* (SIAM, Philadelphia, 2002).
[46]K. R. Castleman, *Digital Image Processing* (Prentice Hall, Englewood Cliffs, NJ, 1996).

[47]Digital image restoration AK, *Digital Image Restoration* (Springer, Berlin, 1991).
[48]B. Jähne, *Digital Image Processing: Concepts, Algorithms, and Scientific Applications*, 5th ed. (Springer, Berlin, 2002).
[49]M. Jiang *et al.*, "Blind deblurring of spiral CT images," IEEE Trans. Med. Imaging **22**, 837–845 (2003).
[50]P. Antich *et al.*, "Application of expectation maximization algorithms for image resolution improvement in a small animal PET system," IEEE Trans. Nucl. Sci. **52**, 684–690 (2005).
[51]I. El Naqa *et al.*, "Improved analysis of PET images for radiation therapy, 14th International Conference on the Use of Computers in Radiation Therapy," Seoul, Korea, 2004, pp. 361–363.
[52]M. Potmesi, "Modeling motion blur in computer-generated images," Comput. Graphics **17**, 389–399 (1983).
[53]T. Zhang *et al.*, "Application of the spirometer in respiratory gated radiotherapy," Med. Phys. **30**, 3165–3171 (2003).
[54]J. M. Balter *et al.*, "Improvement of CT-based treatment-planning models of abdominal targets using static exhale imaging," Int. J. Radiat. Oncol., Biol., Phys. **41**, 939–943 (1998).
[55]A. E. Lujan *et al.*, "A method for incorporating organ motion due to breathing into 3D dose calculations," Med. Phys. **26**, 715–720 (1999).
[56]Y. Seppenwoolde *et al.*, "Precise and real-time measurement of 3D tumor motion in lung due to breathing and heartbeat, measured during radiotherapy," Int. J. Radiat. Oncol., Biol., Phys. **53**, 822–834 (2002).
[57]S. S. Vedam *et al.*, "Predicting respiratory motion for four-dimensional radiotherapy," Med. Phys. **31**, 2274–2283 (2004).
[58]D. A. Low *et al.*, "Novel breathing motion model for radiotherapy," Int. J. Radiat. Oncol., Biol., Phys. **63**, 921–929 (2005).
[59]S. K. Nayar and M. Ben-Ezra, "Motion-based motion deblurring," IEEE Trans. Pattern Anal. Mach. Intell. **26**, 689–698 (2004).
[60]P. Magain, F. Courbin, and S. Sohy, "Deconvolution with correct sampling," Astrophys. J. **494**, 472–477 (1998).
[61]A. K. Katsaggelos, *Digital Image Restoration* (Springer, Berlin, 1991).
[62]A. K. Katsaggelos and K. T. Lay, "Image identification and image restoration based on the expectation-maximization algorithm," Opt. Eng. (Bellingham) **29**, 436–445 (1990).
[63]V. Z. Mesarovic, N. P. Galatsanos, and M. N. Wernick, "Iterative linear minimum mean-square-error image restoration from partially known blur," J. Opt. Soc. Am. A **17**, 711–723 (2000).
[64]T. Fusco *et al.*, "Myopic deconvolution method for adaptive optics images of stellar fields," Astron. Astrophys., Suppl. Ser. **134**, 193–200 (1999).
[65]T. J. Holmes, "Blind deconvolution quantum limited incoherent imagery: Maximum likelihood approach," J. Opt. Soc. Am. A **9**, 1052–1061 (1992).
[66]J. Deasy, V. Wickerhauser, and M. Picard, "Accelerating Monte-Carlo simulations of radiation therapy dose distributions using wavelet threshold denoising," Med. Phys. **29**, 2366–2377 (2002).
[67]J. Fan and J.-Y. Koo, "Wavelet deconvolution," IEEE Trans. Inf. Theory **48**, 734–747 (2002).
[68]I. El Naqa *et al.*, "Compensation of breathing motion artifacts in thoracic PET images by wavelet-based deconvolution," International Symposium on Biomedical Imaging, Arlington, VA, 2006.
[69]J. Starck and E. Pantin, "Deconvolution in Astronomy: A Review," Astron. Soc. Pac. **114**, 1051–1069 (2002).
[70]R. C. Puetter, T. R. Gosnell, and A. Yahil, "Digital image reconstruction: Deblurring and denoising," Annu. Rev. Astron. Astrophys. **43**, 139–194 (2005).
[71]Information technology-Digital compression and coding of continuous tone still images: Requirements and guidelines: International Organization for Standardization (ISO), 2000.
[72]M. V. Wickerhauser, *Adapted Wavelet Analysis from Theory to Software* (Peters, Natick, MA, 1994).
[73]N. P. Galatsanos *et al.*, "Hierarchical Bayesian image restoration from partially known blurs," IEEE Trans. Image Process. **9**, 1784–1797 (2000).
[74]D. L. Donoho and I. M. Johnstone "Adapting to unknown smoothness via wavelet shrinkage," J. Am. Stat. Assoc. **90**, 1200–1224 (1995).
[75]I. El Naqa *et al.*, "A comparison of Monte Carlo dose calculation denoising techniques," Phys. Med. Biol. **50**, 909–922 (2005).
[76]P. M. Bloomfield *et al.*, "The design and implementation of a motion correction scheme for neurological PET," Phys. Med. Biol. 959–978 (2003).
[77]K. Thielemans, S. Mustafovic, and L. Schnorr, "Image reconstruction of motion corrected sinograms," Nuclear Science Symposium Conference Record, 2003 IEEE. 4, 2401–2406 (2003).